Materials Advances

ROYAL SOCIETY OF CHEMISTRY

PAPER

View Article Online
View Journal | View Issue

Open Access Article. Published on 30 June 2021. Downloaded on 10/31/2025 7:40:06 AM.
This article is licensed under a Creative Commons Attribution-NonCommercial 3.0 Unported Licence.

Check for updates

Cite this: *Mater. Adv.*, 2021, **2**, 5494

P-type cobaltite oxide spinels enable efficient electrocatalytic oxygen evolution reaction†

David Doppelbauer,[ab] Abdalaziz Aljabour,[a] Halime Coskun,[a] He Sun,[ac] Markus Gusenbauer,[ab] Julia Lumetzberger,[b] Daniel Primetzhofer,[d] Bogdan Faina,[b] Jiri Duchoslav,[e] Matthias Kehrer,[e] David Stifter,[e] Heiko Groiss,[ef] Verena Ney,[b] Andreas Ney[b] and Philipp Stadler *[ac]

Received 22nd February 2021,
Accepted 17th June 2021

DOI: 10.1039/d1ma00157d

rsc.li/materials-advances

Currently, energy-efficient electrocatalytic oxygen evolution from water involves the use of noble metal oxides. Here, we show that highly p-conducting zinc cobaltite spinel $Zn_{1.2}Co_{1.8}O_{3.5}$ offers an enhanced electrocatalytic activity for oxygen evolution. We refer to previous studies on sputtered Zn–Co spinels with optimized conductivity for implementation as (p-type) transparent conducting oxides. Based on that, we manufacture off-stoichiometric conducting p-spinel catalytic anodes on tetragonal Ti, Au–Ti and hexagonal Al-doped ZnO carriers and report the evolution of O_2 at Tafel slopes between 40.5 and 48 mV dec^{-1} and at overpotentials between 0.35 and 0.43 V (at 10 mA cm^{-2}). The anodic stability, *i.e.*, 50 h of continuous O_2 electrolysis in 1 M KOH, suggests that increasing the conductivity is advantageous for electrolysis, particularly for reducing the ohmic losses and ensuring activity across the entire surface. We conclude by pointing out the merits of improving p-doping in Zn–Co spinels by optimized growth on a tetragonal Ti-carrier and their application as dimension-stable 3d-metal anodes.

1 Introduction

Electrocatalytic water splitting is considered as a viable technology for hydrogen production.[1–3] Alkaline water electrolyzers (AWEs) offer best-in-class energy efficiency to produce hydrogen and oxygen in large quantities.[4] The crucial elements in AWEs are electrocatalytic 3d-metal (oxy)hydroxides and -oxides which are required to reduce the overpotentials of the oxygen evolution reaction (OER) to enable energy-efficient water splitting without the use of scarce and expensive elements. State-of-the-art alkaline-medium catalysts are dominated by Ni–Fe(oxy)hydroxides.[5–7] These abundant catalyst systems achieve an acceptable compromise between overpotentials and anode stabilities; however, they possess inherently poor electrical conductivities that impede the electron flow across a catalyst film and leads to Ohmic losses particularly at high current densities.[8–10] Conductive additives, such as graphene oxide, carbon nanotubes and others, can help in increasing the conductivity and electrocatalytic performance; however, they come at the cost of anodic stabilities.[11–13] Our strategy here is to increase the intrinsic electrical conductivity of the corresponding (electrocatalytic) oxide; hence, we select the zinc cobaltite spinel system (nominal $ZnCo_2O_4$) and seek adaptation in stoichiometry and growth to optimize electroconductivity and thus electrocatalytic OER performance.[14–18] We demonstrate the manufacturing of dimension-stable anodes using a highly p-doped Zn–Co spinel on Ti (and native TiO_2) and Al-doped ZnO conducting carriers. These catalytic systems exhibit a remarkable electrocatalytic performance. We adjust the spinel's Zn : Co ratio towards large p-doping, and increase the oxide conductivity and with that the effective geometric surface activity in the electrolysis; this represents an elementary advantage as compared to the insulating Ni–Fe (oxy)hydroxides; we add that p-doping has been reported to aid the kinetics in the inner Helmholtz plane in alkaline solutions.[8,13,19] Zn–Co spinels can be intensively p-doped by defects, especially in epitaxic off-stoichiometric films grown, *e.g.*, on sapphire. Here, the deposition conditions are decisive to establish p-doped oxides achieving conductivities beyond 1 S cm^{-1}.[20–22] Such conducting spinels are considered as alternative p-type transparent conducting oxides useful in various electronic devices. In this work, we study the adjusted off-stoichiometric growth

[a] *Institute of Physical Chemistry, Johannes Kepler University Linz, Altenbergerstrasse 69, 4040 Linz, Austria. E-mail: philipp.stadler@jku.at*
[b] *Institute of Semiconductor and Solid State Physics, Johannes Kepler University Linz, Altenbergerstrasse 69, 4040 Linz, Austria*
[c] *Linz Institute of Technology, Johannes Kepler University Linz, Altenbergerstrasse 69, 4040 Linz, Austria*
[d] *Department of Physics and Astronomy, Uppsala University, Box 516, 751 20, Uppsala, Sweden*
[e] *Center for Surface and Nanoanalytics, Johannes Kepler University Linz, Altenbergerstrasse 69, 4040 Linz, Austria*
[f] *Christian Doppler Laboratory for Nanoscale Phase Transformations, Center for Surface and Nanoanalytics, Johannes Kepler University Linz, Altenberger Str. 69, 4040 Linz, Austria*

† Electronic supplementary information (ESI) available: Material characterization and electrochemical characterization. See DOI: 10.1039/d1ma00157d

© 2021 The Author(s). Published by the Royal Society of Chemistry

Open Access Article. Published on 30 June 2021. Downloaded on 10/31/2025 7:40:06 AM.
This article is licensed under a Creative Commons Attribution-NonCommercial 3.0 Unported Licence.

of a Zn–Co spinel on titanium (plus native TiO_2) and Al-doped ZnO as (tetragonal and hexagonal) carrier substrates. In addition, we refer to previous studies, where p-doped spinels were grown by reactive magnetron sputtering (RMS) from ZnO/Co_3O_4 targets on sapphire (0001). This technique enables a precise control of the p-doping by matching the target composition (Zn : Co) with the resulting Zn–Co spinels at Zn : Co equal to 0.66 (2 : 3).[23] This ratio is 30% of the nominal spinel ($ZnCo_2O_4$, Zn : Co = 0.5) and induces the desired off-stoichiometry in the spinel with a hole carrier density typically beyond 1×10^{21} cm^{-3}. We reproduce this work on sapphire (0001) and report a hole density of 1.5×10^{21} cm^{-3} and an electrical conductivity of 6.1 S cm^{-1} as measured by 4-probe resistivity and Hall measurements. Based on this, we employed these parameters on a titanium mesh (Ti-mesh with native TiO_2) and Al-doped ZnO (Al:ZnO). For comparison, we grow control spinels on sapphire (0001) and rutile (TiO_2) to study the exact impact of the underlying substrate. We report that the Ti-mesh and Al:ZnO lead to spinels with different quality. While on tetragonal TiO_2, the growth is similar to that of sapphire (0001) (and the control samples on rutile), and wurtzite (Al:ZnO) obviously induces larger polycrystallinity. This is also reflected in the OER electrolysis, where the spinel on the Ti-mesh shows a state-of-the-art electrocatalytic performance with a Tafel slope and an overpotential as low as 40.5 mV dec^{-1} and 0.35 V (at 10 mA cm^{-2}), respectively, and a turn-over frequency (TOF) as high as 0.07 s^{-1}, while on Al:ZnO, we observed a 0.08 V larger overpotential, but a similar Tafel slope; hence, we relate the minor activity to the poorer crystalline quality. We further studied the spinel on a 10-nm Au-covered Ti-mesh, in order to exclude the corrosion effects on the Ti mesh under large anodic bias. These anodes show a remarkable stability, but the Au-interlayer increases the spinel's overpotentials and Tafel slopes. In summary, our Zn–Co spinel/Ti-anodes are suitable for long-term continuous OER electrolysis and demonstrate that RMS-deposition is useful to obtain quasi-epitaxic p-doped Zn–Co spinels on titanium as dimension-stable electrocatalytic anodes.[24–26] We report that the influence of the carrier substrate is decisive, particularly the tetragonal rutile systems impact the growth of the spinel oxide positively, while wurtzite, here exemplified with Al:ZnO, is less appropriate. This is further indicated by the performance of a few nanometer Au-covered Ti-mesh, where the overpotentials and Tafel slopes increased slightly. As such, this work shows that Zn–Co spinels render stable electrocatalytic anodes when combined with titanium. These systems are suitable for electrolysis at high current densities without notable Ohmic losses.[8,27,28]

2 Results and discussion

Zn–Co spinels are deposited by reactive magnetron sputtering (RMS) in the presence of an Ar–O_2 gas blend (Ar : O_2 = 10 : 0.5 sccm) at a pressure of 4×10^{-3} mbar. The temperature and magnetron power are set to 623 K and 30 W, respectively. We grow thin films at nominal 200 nm thickness. The exact thickness varies between 160 and 200 nm as measured by X-ray reflectometry and profilometry. Zn–Co spinels are grown on the *c*-plane sapphire Al_2O_3 (0001) serving as reference substrates to perform bulk structural analysis by Rutherford backscattering (RBS) and bulk electrical transport by 4-probe resistivity/Hall measurements. For the electrocatalytic anodes, spinels are grown on a Ti-mesh with a native TiO_2 including reference samples on TiO_2 (rutile) to study the deposition on TiO_2, and on Al-doped ZnO (Al:ZnO) to study the deposition on sapphire to elucidate the electrocatalytic performance on different carrier substrates. The corresponding schematics of the Ti-mesh, electrochemical cell and related electrochemical reference measurements for Al:ZnO and Ti-mesh are included in the ESI† (Fig. S1–S4). The RMS preparation conditions, *i.e.*, Ar : O_2 = 10 : 0.5 sccm flow ratio, 623 K at 30 W power, were employed to yield systematically Zn–Co spinels with a stoichiometry composition of $Zn_{1.2}Co_{1.8}O_{3.5}$, as measured by Rutherford backscattering spectrometry (RBS, Fig. 1a and b). We use a primary ion energy of 2 MeV He^+ and for comparison, we use 10 MeV C^{3+} to obtain the bulk composition. The resulting stoichiometry is derived from an itinerary fit. The Zn : Co ratio is thereby 0.65, consistent with the target composition (ZnO to Co_3O_4 at 2 : 3 during sputtering). The excess of Zn and the deficiency of O correspond to strong defect doping which is the characteristic of Zn–Co spinels.[22] The presence of large antisites, *i.e.*, varying positions among Zn^{2+} : Co^{2+} : Co^{3+}, has been reported earlier.[22] Off-stoichiometries, as shown here, lead to strong p-doping. We denote that a similar composition of the surface is obtained using Auger–Meitner electron spectroscopy (AES, Fig. 4d).

In parallel, we study the electrical transport of the as-deposited $Zn_{1.2}Co_{1.8}O_{3.5}$ by 4-probe resistivity and Hall measurements (Fig. 2a and b). The samples show a conductivity as high as 6.1 S cm^{-1} with a hole density of 1.5×10^{21} cm^{-3} and mobility of 0.025 cm^2 V^{-1} s^{-1} at 300 K. The temperature coefficient of resistivity is negative and has an activation energy of 65 meV (Fig. 2a, inset). A similar transport profile is reported in Zn–Co spinels grown by pulsed laser deposition (PLD).[31–33] In general, the mobility values of p-type PLD- and RMS-grown Zn–Co spinels are comparatively low, which is related to the

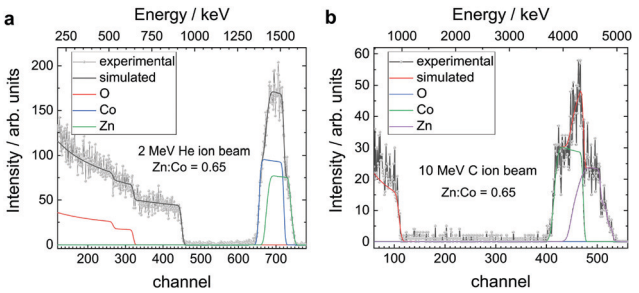

Fig. 1 $Zn_{1.2}Co_{1.8}O_{3.5}$ composition characterization. (a) Rutherford backscattering spectrometry (RBS, here: primary ion energy at 2 MeV He^+) shows the (bulk) Zn : Co ratio of the as-deposited Zn–Co spinel oxide at 0.65. The analysis is conducted according to an itinerary fit.[29,30] (b) The ratio of the composition metal constituents, as well as the homogeneity of their respective concentration, is additionally checked by RBS using 10 MeV C^{3+} ions. In summary, the bulk structure composition for the Zn–Co spinel grown by RMS corresponds to the stoichiometry of $Zn_{1.2}Co_{1.8}O_{3.5}$.

Open Access Article. Published on 30 June 2021. Downloaded on 10/31/2025 7:40:06 AM.
This article is licensed under a Creative Commons Attribution-NonCommercial 3.0 Unported Licence.

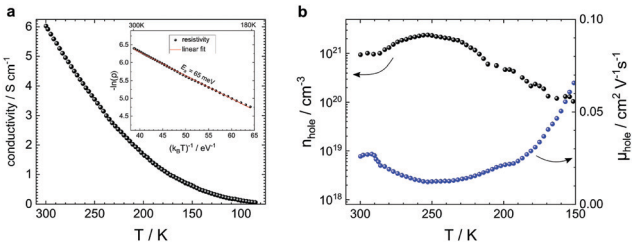

Fig. 2 $Zn_{1.2}Co_{1.8}O_{3.5}$ electrical transport characterization. (a) Bulk conductivity *versus* temperature of a 193-nm Zn–Co spinel on sapphire shows a negative temperature coefficient of resistivity with an activation energy of 65 meV (inset). (b) Hall measurements (van der Pauw method) reveal a hole carrier density of above 10^{21} cm^{-3} and a mobility of 0.025 cm^2 V^{-1} s^{-1}.

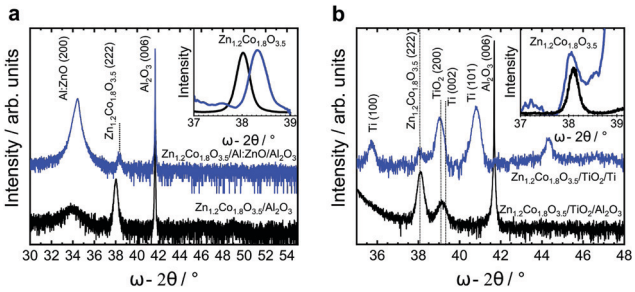

Fig. 3 X-ray diffraction pattern of $Zn_{1.2}Co_{1.8}O_{3.5}$. Diffraction pattern of Zn–Co spinel on (a) sapphire and Al:ZnO/sapphire. The spinel (222) reflection at 38° (2Θ) shifts by +0.3° on Al:ZnO (normalized zoom in the inset). The peak broadened on Al:ZnO indicating larger tensions/defects from the lattice mismatch wurtzite/spinel as compared to sapphire/spinel. (b) Growth of Zn–Co spinels on rutile TiO_2/sapphire and on a Ti-mesh with native TiO_2. Both peaks are comparable to the sapphire reference. On Al:ZnO, the large lattice mismatch wurtzite/spinel leads to a broader and less intense diffraction pattern.

strong presence of defects and the polycrystallinity of the sample. Here, the lattice mismatch between the spinel and the substrates (sapphire, TiO_2, Al:ZnO, *etc.*) plays a major role. Table 1 summarizes the electrical parameters including a comparison with the discussed state-of-the-art performance. We denote that the RMS mobilities and conductivities of this work are superior to those of the PLD-grown spinels. Superior mobilities and conductivities are only obtained from spinel–spinel lattice-matched epitaxic stacks ($MgAl_2O_4$/Zn–Co spinel).[22]

The low mobility and lattice mismatch implement tensions in the spinel structure emerging from the substrate. We present here the diffraction patterns of spinels grown on different potential carrier electrodes and the corresponding reference substrates: spinels on sapphire and sapphire/TiO_2 for reference; spinels on a Ti-mesh with native TiO_2 and sapphire/Al:ZnO. All these substrates lead to an oxide with a characteristic fingerprint (222) diffraction pattern. However, these substrates induce a different peak intensity and width. The full width at half maximum (FWHM, insets Fig. 3a and b) allows the estimation of the average grain size using the Scherrer formula. The spinel/sapphire and spinel/TiO_2 show an equal or similar diffraction pattern and an average grain size of ≈30 nm. This pattern is slightly broadened on the Ti-mesh (FWHM = 0.28°) and yields a relative average grain size of 28.6 nm. A substantial shift/broadening is observed on the spinel/Al:ZnO (approx. FWHM at 0.39° corresponding to the 21 nm average grain size and the smallest relative (222) spinel intensity). We conclude that while Al:ZnO (wurtzite) has a detrimental impact on the spinel, the sapphire, TiO_2 and Ti-mesh (with native oxide) lead to practically equal growth (Table 2 and ESI,† Table S1, Fig. S7). To study the OER, we manufacture electrocatalytic anodes using $Zn_{1.2}Co_{1.8}O_{3.5}$ deposited on the Ti-mesh and Al:ZnO in 1 M KOH (pH = 13.96) as the electrolyte. We perform cyclic voltammetry and chronoamperometry to explore the O_2 evolution and the relative stability over time using the electrochemical half-cell (anode space separated with a glass frit, ESI,† Fig. S13). As the reference electrode we deploy an electrolyte-matched Hg|HgO|1 M KOH‖ system calibrated at +0.098 V *vs.* SHE. As the counter electrode (in the cathode space) we use Ni. The spinel-covered Ti-meshes and the Al:ZnO/sapphire substrates are mounted in the anode space. Linear sweep voltammetry and chronoamperometry are performed under stirring or flow (for the Al:ZnO system, a corresponding cell is designed to bury the KOH-sensitive Al:ZnO completely underneath the active spinel). In addition, we conduct reference cyclic voltammetry and chronoamperometry on a plane Ti-mesh without spinels. The active area of the Ti-mesh is calculated according to the surface-volume factor of the mesh (a factor of 0.75 compared to the projected plate area, ESI,† Fig. S2). This value is confirmed by probing the dimension using scanning electron microscopy. The active area of the spinel/Al:ZnO is directly measured (a ring with a radius of 2.5 mm). The cyclic voltammetry is swept at a constant ratio with a repeating factor of 50 cycles between 10 and 50 mV s^{-1}. The scans show the increase of the electrocatalytic current to 10 mA cm^{-2} at an overpotential as low as 0.35 V and a Tafel slope as low as 40.5 mV dec^{-1} (CVs, Fig. 4a and Tafel analysis, Fig. 4c). The activity of the (nominally) 200-nm thin film remains stable after several hours of continuous evolution of O_2 (Fig. 4b). Similar results at slightly higher overpotentials are observed for the Al:ZnO/sapphire using a flow cell. Here, the overpotential at 10 mA cm^{-2} reaches 0.43 V with a Tafel slope at 42.2 mV dec^{-1} (summary in Table 3). We denote that the spinel/Al:ZnO electrode shows a gradual

Table 1 Electrical parameters of polycrystalline p-type Co-spinels

System	Method	σ/S cm^{-1}	n_{hole}/cm^{-3}	μ_H/cm^2 V^{-1} s^{-1}	Ref.
$Zn_{1.2}Co_{1.8}O_{3.5}$	RMS	6.2	1.5×10^{21}	0.026	This work
$Zn_xCo_{3-x}O_4$	PLD	5	$0.5–2 \times 10^{21}$	0.01–0.06	Schein *et al.*[34]
$Zn_xCo_{3-x}O_4$	Epitaxic PLD[a]	35–110	$5–6 \times 10^{21}$	0.043–0.115	Huang *et al.*[22]
Co_3O_4	CVD, ΔT	10^{-2}	—	—	Cheng *et al.*[35]

[a] Epitaxic $ZnCo_2O_4$–$MgAl_2O_4$ PLD stacks.

 © 2021 The Author(s). Published by the Royal Society of Chemistry

Open Access Article. Published on 30 June 2021. Downloaded on 10/31/2025 7:40:06 AM.
This article is licensed under a Creative Commons Attribution-NonCommercial 3.0 Unported Licence.

Table 2 Structural parameters of polycrystalline p-doped Zn–Co spinels

Substrate	Crystal family	Peak spinel (222)/2θ (deg)	FWHM/ 2θ (deg)	τ^a/nm
Sapphire (0001)	Hexagonal	38.0	0.25	31.8
Rutile	Tetragonal	38.092	0.25	32
Ti-Mesh (native TiO_2)	Tetragonal	38.092	0.28	28.6
Al:ZnO (wurtzite)	Hexagonal	38.3	0.39	21

[a] Scherrer analysis with λ = 0.15406 nm (Cu $K_{\alpha 1}$) and shape factor K = 0.89 (spherical).

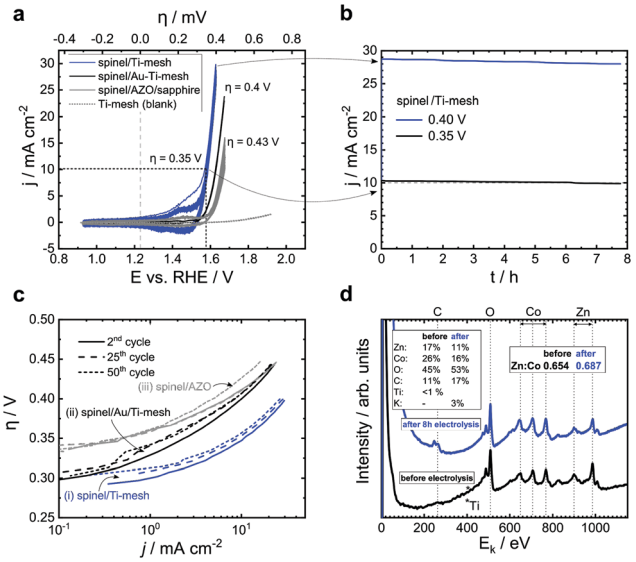

Fig. 4 Electrocatalytic performance and stability analysis of p-doped conducting spinel $Zn_{1.2}Co_{1.8}O_{3.5}$ on (i) Ti-mesh, (ii) Au-covered Ti-Mesh and (iii) Al-doped ZnO (AL:ZnO). (a) Cyclic voltammograms with 50 repeats at 50 mV s^{-1} in 1 M KOH (reference electrode Hg|HgO|1 M KOH‖ at +0.098 V *vs.* SHE) and (b) chronoamperometric (j_{anodic}) scans of the superior spinel/Ti-mesh for 8 h at 0.35 and 0.4 V overpotentials. (c) Electrocatalytic Tafel performance including change by time (dashed lines show the 25th and 50th cycles). The Tafel slopes correspond to 40.5 (spinel/Ti-mesh), 48.5 (spinel/Au/Ti-mesh) and 42.2 mV dec^{-1} (spinel/Al:ZnO), respectively. The slopes are extracted from the linear regime between 0.1 and 1 mA cm^{-2}, ESI,† Fig. S13. (d) Auger–Meitner electron spectroscopy (AES) before and after 8 h of OER electrolysis on spinel/Ti-mesh. The composition after electrolysis indicates a relative increase of Zn, *i.e.*, the Zn–Co spinel loses a minor amount of Co-moieties during electrolysis. The surface composition before electrolysis is in agreement with the RBS from Fig. 1.

decomposition in 1 M KOH. The parallel conducted chronoamperometric scans of the Ti-mesh show that the present configuration allows testing over several hours under stable currents. We confirm the stability of the electrocatalyst by crosschecking the Auger–Meitner photoelectron pattern (AES, recorded *ex situ* before and after electrolysis, Fig. 4d). The Zn content decreases on the surface, *i.e.*, the Zn : Co decreases from 0.65 to 0.62. We denote that the surface is contaminated with the residual electrolyte (K-peak and increasing carbonate from exposure to ambient air). In long-term measurements, we also take the anodic corrosion of the Ti-mesh into account. Since we observe the growth of TiO_2 after multiple scans (ESI,† Fig. S12), we sandwich a thin Au-layer between the spinel and the Ti-mesh. The interlayer leads to an increased overpotential of 0.4 V (*i.e.* +0.05 V) beyond the plane Ti-mesh (Fig. 4a and ESI,† Fig. S11), but allows us to perform 50 h of continuous O_2 electrolysis with suppressed Ti-TiO_2 corrosion. Here, the Faraday currents gradually decrease by 5% compared to the initial value which proves the stability of the Zn–Co spinel (CV and chronoamperometry of Ti/Au in the ESI,† Fig. S11). In general, the Au-covered Ti-mesh shows results similar to the Ti-mesh (Tafel slopes are almost equal). The electrocatalytic performance on Al:ZnO is lower as compared to that on the Ti-mesh. We refer here to the XRD study and the poorer signal quality of the spinel on Al:ZnO indicating a larger polycrystallinity. In combination, these results show that the native TiO_2 on the Ti-mesh allows the growth of epitaxic $Zn_{1.2}Co_{1.8}O_{3.5}$ on sapphire or rutile, while the lattice mismatch limits the application of spinel/Al:ZnO. In combination, spinel on titanium (and TiO_2) is attractive for electrocatalytic anodes. Particularly by optimized growth, shown here using sputtering, p-doped spinels unfold a state-of-the-art electrocatalytic performance, and in view of their intrinsic conductivity, they can serve as attractive electrocatalytic oxides for large-scale OER electrocatalysis performed at high current densities.

Table 3 $Zn_{1.2}Co_{1.8}O_{3.5}$ performance in 1 M KOH: Tafel slope and overpotentials (η) at 298 K on different substrates as compared to NiFe hydroxides under similar conditions

Anode stack	Tafel slope/ mV dec^{-1}	η/V	Load[b]/ µg cm^{-2}	TOF[a]/s^{-1}	Ref.
Spinel/Ti-mesh	40.5	0.35	90	0.07	This work
Spinel/Au–Ti-mesh	48.5	0.4	90	0.02	This work
Spinel/Al:ZnO	42.2	0.43	180	<0.01	This work
NiFe-LDH[c]/GC[d]	67	0.347	70	0.01	10
3D-NiFe-LDH/Ni	50	0.250	1000	0.028	9
Ni–Fe/Au	58	0.331	140	—	36

[a] At η = 0.35 V. [b] Electrocatalyst load mass. [c] Layered double hydroxide. [d] Glassy carbon.

3 Conclusions

In summary, we show that the reactive magnetron sputtering from ZnO/Co_3O_4 (2 : 3) targets leads to the growth of p-type conducting Zn–Co spinels with the composition of $Zn_{1.2}Co_{1.8}O_{3.5}$. This oxide is deposited on a Ti-mesh (with native TiO_2) and Al:ZnO, and for comparison, on sapphire and TiO_2 (rutile), to elucidate the impact of the substrate. We find that the growth on TiO_2 is similar to that on sapphire. This can be used to manufacture electrocatalytic anodes based on Ti-meshes with native TiO_2 and spinels that exhibit a state-of-the-art electrocatalytic OER performance as compared to that of common alkaline electrocatalyst systems. Furthermore, we manufacture anodes from spinels grown on Al-doped ZnO and show that the poorer structural quality leads to lower electrocatalytic performance. We conclude by pointing out the merit of reactive magnetron sputtering to obtain zinc-rich, p-conducting spinels for the OER directly deposited on a Ti-mesh at moderate temperatures. We find that the growth on the Ti-mesh with its (rutile) TiO_2 layer is beneficial for

Open Access Article. Published on 30 June 2021. Downloaded on 10/31/2025 7:40:06 AM.
This article is licensed under a Creative Commons Attribution-NonCommercial 3.0 Unported Licence.

columnar spinel growth to ultimately demonstrate dimension-stable anodes for the OER. In this sense, the work here is inspired by the high conductivities of the corresponding Zn-based ternary spinels $ZnRu_2O_4$ and $ZnIr_2O_4$,[31,37–40] *i.e.*, to seek improvement in the electrical conductivity for 3d-metal oxides as one path to improve the OER on titanium carriers.

4 Experimental section

4.1 RMS growth of spinel-type $Zn_{1.2}Co_{1.8}O_{3.5}$

The spinel-type $Zn_{1.2}Co_{1.8}O_{3.5}$ was grown in an ultra-high vacuum (UHV) chamber (base pressure $\sim 2 \times 10^{-9}$ mbar) by reactive magnetron sputtering (RMS) from a ZnO/Co_3O_4 (2 : 3) target onto a heated substrate (heating temperature $T_H = 623$ K) with an argon-to-oxygen ratio (purity: 6N) of $Ar : O_2 = 10 : 0.5$ standard cubic centimeter per minute at a working/deposition pressure of 4×10^{-3} mbar with a magnetron power of 30 W. Under these conditions, the sputter rate usually is around 3.5 nm min^{-1}.[23] The thickness of the deposited $Zn_{1.2}Co_{1.8}O_{3.5}$ was measured by X-ray reflectivity (Fig. S10, ESI†).

Hall measurements. The electrical measurements of $Zn_{1.2}Co_{1.8}O_{3.5}$ (on c-sapphire, Al_2O_3 (0001), CrysTec GmbH) were performed in a van der Pauw configuration between 70 K and 300 K. 193 nm films on 1×1 cm^2 sapphire were contacted using indium/gold leads. The measurements were carried out at pressures in the 10^{-5} mbar range. The sample holder was connected to a refrigerator-cooled cryostat (Leybold-Heraeus RNK 10–300 and LakeShore Cryotronics 8400 Series HMS). The Hall constant and resistivity were measured under a maximum magnetic field of 0.91 T (AC and DC mode) and a current of 1 mA. Details of the Hall parameters are presented in the ESI† (Fig. S18–S21).

Ion beam analysis. The composition of the Zn–Co spinel oxide was determined accurately by ion beam analysis. For this, we deployed Rutherford backscattering spectrometry (RBS) using 2 MeV He^+ as well as 10 MeV $^{12}C^{3+}$ primary beams at the Tandem Laboratory at Uppsala University. To disentangle the element-specific contributions, the spectra were analyzed using SIMNRA software.[29] Details of the experimental setup are described elsewhere.[30] The complementary comparison of the 2 MeV He^+ and 10 MeV $^{12}C^{3+}$ primary beams led to the bulk stoichiometric composition of Zn : Co : O in summary, which is $Zn_{1.2}Co_{1.8}O_{3.5}$. We show that the penetration depth of the ion beams exceeds the thickness of the film (150 nm).

Auger–Meitner electron spectroscopy. The Auger–Meitner electron spectroscopy (AES) measurements were performed using a scanning AES microscope JAMP-9500 F (JEOL, JP) equipped with a hemispherical electron energy analyzer and a channeltron detector. The AES spectra were recorded with an acceleration voltage of 10 kV and an electron beam current of 20 nA, which resulted in a diameter of approximately 30 nm for the measurement spot.

X-ray diffraction and TEM. In order to probe the crystal properties of the grown films, XRD was performed with an X'Pert PRO PANalytical MRD diffractometer. The X-ray source consists of a copper anode ($K_{\alpha 1}$, $\lambda = 0.15406$ nm) with hybrid two-crystal Germanium (220) Bartels type beam optics. The diffractograms were recorded with a voltage of 40 kV and an anode current of 40 mA. The reference and extended diffractograms are presented in the ESI† (Fig. S5–S7).

The structure of the $Zn_{1.2}Co_{1.8}O_{3.5}$/Ti-mesh was investigated using (scanning) transmission electron microscopy (TEM). An overview of the layer system (Fig. S8 and S9) shows the Ti-mesh covered by layered TiO_2 with varying thickness (20 to 100 nm) and on top of $Zn_{1.2}Co_{1.8}O_{3.5}$ with a homogeneous thickness of ≈ 150 nm. For the TEM sample preparation, the active layer was covered with Pt deposition to protect it during FIB (focused ion-beam) cutting. The $Zn_{1.2}Co_{1.8}O_{3.5}$ consists of thin columnar grains with different diameters in the range of 10–40 nm (Fig. 3c). A rough statistic from 20 measured grains leads to an average domain size (τ) of 24 nm (in agreement with the Scherrer analysis, Fig. S5–S7 and Table 2). Most of the columns reach from the TiO_2 to the top of the layer. The crystallinity of these columnar $Zn_{1.2}Co_{1.8}O_{3.5}$ grains was additionally proven by phase contrast imaging performed by conventional TEM (ESI,† Fig. S8 and S9). Focused ion beam (FIB) cutting with a CrossBeam 1540 XB (ZEISS, Germany) was used to prepare the thin cross-sectional lamella for the TEM investigation. Several layers of electron and ion beam Pt deposition have been used for surface protection. The FIB was operated at 30 kV for sample cutting and lift-out. To achieve a high lamella quality and to reduce the amorphization of the sample, a Ga acceleration voltage of 5 kV was used for final thinning. The scanning and conventional transmission electron microscopy (TEM) investigation was performed using a JEM-2200FS (JEOL, Japan operated at an acceleration voltage of 200 kV).

Electrochemical measurements. For the evaluation of the electrocatalytic performance, a conventional H-cell with a three-electrode configuration was used. $Zn_{1.2}Co_{1.8}O_{3.5}$ on a titanium mesh (Goodfellow, 5N-Ti, size 1×1 cm^2, aspect ratio 0.75 : 1, effective area 0.75 cm^2, SEM picture in the ESI,† Fig. S2 and S16) carrier electrode served as the working electrode (WE), whereas the counter electrode (CE) consisted of a (much larger) nickel plate. The highly alkaline 1 M KOH (purity: 85%, Alfa Aesar) electrolyte requires the use of an (electrolyte-matched) Hg|HgO|1 M KOH‖ reference electrode (RE). A HANNA Instruments pH 211 microprocessor pH-meter was used to measure the pH values of the electrolyte. The solution in the WE compartment was stirred with a magnetic stirrer ($\sim$350 rpm). In this cell configuration, oxygen evolution took place in the WE and hydrogen evolution in the CE compartment, which are separated using a glass frit (Fig. S17, ESI†). The RE was placed close to the WE. Its standard electrode potential is $E^0_{Hg|HgO} = +0.098$ V *versus* the standard hydrogen electrode (*vs.* SHE). Therefore, the measured potential *versus* the reversible hydrogen electrode (RHE) is:

$$E_{RHE} = E_{Hg|HgO} + 0.098V + 0.0591V{\cdot}pH. \quad (1)$$

The electrochemical measurements were performed with a JAISSLE potentiostat/galvanostat IMP 88 PC. Electrochemical

 © 2021 The Author(s). Published by the Royal Society of Chemistry

Open Access Article. Published on 30 June 2021. Downloaded on 10/31/2025 7:40:06 AM.
This article is licensed under a Creative Commons Attribution-NonCommercial 3.0 Unported Licence.

impedance spectroscopy was used to determine the cell parameters by applying an AC voltage with an amplitude of 50 mV in the range from 0.1 Hz to 100 kHz. The measurement allowed the determination of the electrolyte, sample and membrane resistances (R_e, R_s and R_m, respectively) (ESI,† Table S2 and Fig. S14) as well as the electrochemical surface area with *j vs.* scan rate (Fig. S16, ESI†). The recorded currents during cyclic voltammetry were normalized to the electrochemical surface area. The geometric surface area was determined from the SEM measurements which yielded a ratio of 0.75 (0.75 cm^2 active area per 1 cm^2 mesh) including purity crosscheck and elemental analysis after electrolysis by X-ray/Auger–Meitner photoelectron spectroscopy (Fig. S2, S4d and S19, ESI†). All voltammograms (cyclic, Tafel slope) were derived from the scans conducted at 10 mV s^{-1}. The headspace gas was analyzed by gas-chromatography (presence of O_2, Fig. S24, ESI†) to calculate the Faraday yield for hydrogen and oxygen. We found quantitative yields close to 98%. The statistical evaluation of the different experiments on the electrocatalytic activity of $Zn_{1.2}Co_{1.8}O_{3.5}$ and high current density (>500 mA cm^{-2}) data are included in the ESI† (Table S3 and Fig. S18, S15).

Conflicts of interest

There are no conflicts to declare.

Acknowledgements

The authors acknowledge the financial support from the Austrian Science Foundation (FWF I3822-N37, Sustainable Catalysis and P26164-N20), the Linz Institute of Technology (LIT, LIT-2017-4-YOU-005, biopolymer-based carbonate reduction) at the Johannes Kepler University Linz, the European Regional Development Fund (EFRE, IWB2014-2020, 2018-98299 Artificial Food and project BIOCARB-K), and the Government of Upper Austria. The authors gratefully acknowledge VR-RFI (Contract No. 2017-00646 9) and the Swedish Foundation for Strategic Research (SSF, Contract No. RIF14-0053) for supporting accelerator operation at Uppsala University (Sweden). The financial support from the Austrian Federal Ministry for Digital and Economic Affairs, the National Foundation for Research, Technology and Development, and the Christian Doppler Research Association is gratefully acknowledged. The authors thank Günter Hesser for TEM sample preparation and fruitful discussions.

Notes and references

1 N.-T. Suen, S.-F. Hung, Q. Quan, N. Zhang, Y.-J. Xu and H. M. Chen, *Chem. Soc. Rev.*, 2017, **46**, 337–365.
2 I. C. Man, H. Su, F. Calle-Vallejo, H. A. Hansen, J. I. Martínez, N. G. Inoglu, J. Kitchin, T. F. Jaramillo, J. K. Nørskov and J. Rossmeisl, *ChemCatChem*, 2011, **3**, 1159–1165.
3 I. Katsounaros, S. Cherevko, A. R. Zeradjanin and K. J. J. Mayrhofer, *Angew. Chem., Int. Ed.*, 2014, **53**, 102–121.
4 C. C. L. McCrory, S. Jung, J. C. Peters and T. F. Jaramillo, *J. Am. Chem. Soc.*, 2013, **135**, 16977–16987.
5 J. Mohammed-Ibrahim, *J. Power Sources*, 2020, **448**, 227375.
6 J. Mohammed-Ibrahim, *J. Power Sources*, 2020, **448**, 227375.
7 R. Chen, S. Hung, D. Zhou, J. Gao, C. Yang, H. Tao, H. B. Yang, L. Zhang, L. Zhang, Q. Xiong, H. M. Chen and B. Liu, *Adv. Mater.*, 2019, **31**, 1903909.
8 Y. Matsumoto and E. Sato, *Mater. Chem. Phys.*, 1986, **14**, 397–426.
9 L. Yu, H. Zhou, J. Sun, I. K. Mishra, D. Luo, F. Yu, Y. Yu, S. Chen and Z. Ren, *J. Mater. Chem. A*, 2018, **6**, 13619–13623.
10 C. Peng, N. Ran, G. Wan, W. Zhao, Z. Kuang, Z. Lu, C. Sun, J. Liu, L. Wang and H. Chen, *ChemSusChem*, 2020, **13**, 811–818.
11 X. Long, J. Li, S. Xiao, K. Yan, Z. Wang, H. Chen and S. Yang, *Angew. Chem.*, 2014, **126**, 7714–7718.
12 M. Gong, Y. Li, H. Wang, Y. Liang, J. Z. Wu, J. Zhou, J. Wang, T. Regier, F. Wei and H. Dai, *J. Am. Chem. Soc.*, 2013, **135**, 8452–8455.
13 D. M. Morales, S. Barwe, E. Vasile, C. Andronescu and W. Schuhmann, *ChemPhysChem*, 2019, **20**, 3030–3036.
14 N. Manca, D. J. Groenendijk, I. Pallecchi, C. Autieri, L. M. K. Tang, F. Telesio, G. Mattoni, A. McCollam, S. Picozzi and A. D. Caviglia, *Phys. Rev. B*, 2018, **97**, 081105.
15 E. Fabbri, A. Habereder, K. Waltar, R. Kötz and T. J. Schmidt, *Catal. Sci. Technol.*, 2014, **4**, 3800–3821.
16 T. W. Kim, M. A. Woo, M. Regis and K.-S. Choi, *J. Phys. Chem. Lett.*, 2014, **5**, 2370–2374.
17 S. Han, S. Liu, R. Wang, X. Liu, L. Bai and Z. He, *ACS Appl. Mater. Interfaces*, 2017, **9**, 17186–17194.
18 X. Liu, Z. Chang, L. Luo, T. Xu, X. Lei, J. Liu and X. Sun, *Chem. Mater.*, 2014, **26**, 1889–1895.
19 P. W. Menezes, A. Indra, A. Bergmann, P. Chernev, C. Walter, H. Dau, P. Strasser and M. Driess, *J. Mater. Chem. A*, 2016, **4**, 10014–10022.
20 M. Stoica and C. S. Lo, *New J. Phys.*, 2014, **16**, 055011.
21 Y. Shi, P. F. Ndione, L. Y. Lim, D. Sokaras, T.-C. Weng, A. R. Nagaraja, A. G. Karydas, J. D. Perkins, T. O. Mason, D. S. Ginley, A. Zunger and M. F. Toney, *Chem. Mater.*, 2014, **26**, 1867–1873.
22 X. C. Huang, J. Y. Zhang, M. Wu, S. Zhang, H. Y. Xiao, W. Q. Han, T.-L. Lee, A. Tadich, D.-C. Qi, L. Qiao, L. Chen and K. H. L. Zhang, *Phys. Rev. B*, 2019, **100**, 115301.
23 B. Henne, V. Ney, K. Ollefs, F. Wilhelm, A. Rogalev and A. Ney, *Sci. Rep.*, 2015, **5**, 16863.
24 T. Reier, I. Weidinger, P. Hildebrandt, R. Kraehnert and P. Strasser, *ECS Trans.*, 2013, **58**, 39–51.
25 T. Reier, D. Teschner, T. Lunkenbein, A. Bergmann, S. Selve, R. Kraehnert, R. Schlögl and P. Strasser, *J. Electrochem. Soc.*, 2014, **161**, F876–F882.
26 B. Johnson, F. Girgsdies, G. Weinberg, D. Rosenthal, A. Knop-Gericke, R. Schlögl, T. Reier and P. Strasser, *J. Phys. Chem. C*, 2013, **117**, 25443–25450.
27 C. Iwakura, M. Nishioka and H. Tamura, *Nippon Kagaku Kaishi*, 1982, 1136–1140.

Open Access Article. Published on 30 June 2021. Downloaded on 10/31/2025 7:40:06 AM.
This article is licensed under a Creative Commons Attribution-NonCommercial 3.0 Unported Licence.

28 J. A. Koza, Z. He, A. S. Miller and J. A. Switzer, *Chem. Mater.*, 2012, **24**, 3567–3573.
29 M. Mayer, *SIMNRA User's Guide*, 2017, https://home.mpcdf.mpg.de/mam/SIMNRA-Users-Guide.pdf.
30 M. Moro, R. Holeňák, L. Zendejas Medina, U. Jansson and D. Primetzhofer, *Thin Solid Films*, 2019, **686**, 137416.
31 M. N. Amini, H. Dixit, R. Saniz, D. Lamoen and B. Partoens, *Phys. Chem. Chem. Phys.*, 2014, **16**, 2588.
32 J. D. Perkins, T. R. Paudel, A. Zakutayev, P. F. Ndione, P. A. Parilla, D. L. Young, S. Lany, D. S. Ginley, A. Zunger, N. H. Perry, Y. Tang, M. Grayson, T. O. Mason, J. S. Bettinger, Y. Shi and M. F. Toney, *Phys. Rev. B: Condens. Matter Mater. Phys.*, 2011, **84**, 205207.
33 H. J. Kim, I. C. Song, J. H. Sim, H. Kim, D. Kim, Y. E. Ihm and W. K. Choo, *J. Appl. Phys.*, 2004, **95**, 7387–7389.
34 F.-L. Schein, M. Winter, T. Böntgen, H. von Wenckstern and M. Grundmann, *Appl. Phys. Lett.*, 2014, **104**, 022104.
35 C.-S. Cheng, M. Serizawa, H. Sakata and T. Hirayama, *Mater. Chem. Phys.*, 1998, **53**, 225–230.
36 X. Yu, M. Zhang, W. Yuan and G. Shi, *J. Mater. Chem. A*, 2015, **3**, 6921–6928.
37 L. C. Seitz, C. F. Dickens, K. Nishio, Y. Hikita, J. Montoya, A. Doyle, C. Kirk, A. Vojvodic, H. Y. Hwang, J. K. Norskov and T. F. Jaramillo, *Science*, 2016, **353**, 1011–1014.
38 J. A. Gauthier, C. F. Dickens, L. D. Chen, A. D. Doyle and J. K. Nørskov, *J. Phys. Chem. C*, 2017, **121**, 11455–11463.
39 Y. Lee, J. Suntivich, K. J. May, E. E. Perry and Y. Shao-Horn, *J. Phys. Chem. Lett.*, 2012, **3**, 399–404.
40 K. A. Stoerzinger, L. Qiao, M. D. Biegalski and Y. Shao-Horn, *J. Phys. Chem. Lett.*, 2014, **5**, 1636–1641.

 © 2021 The Author(s). Published by the Royal Society of Chemistry